

Instrument line shape modeling and correction for off-axis detectors in Fourier transform spectrometry

Kevin W. Bowman, Helen M. Worden, Reinhard Beer
Jet Propulsion Laboratory

August 11, 1999

Abstract

Spectra measured by off-axis detectors in a high-resolution Fourier transform spectrometer (FTS) are characterized by frequency scaling, asymmetry and broadening of their line shape, and self-apodization in the corresponding interferogram. For a narrow-band input spectrum and a specified detector geometry, a formalism is presented that accounts for these effects with separate terms. Some of the terms are used to correct the larger off-axis effects as part of calibration. The remaining terms are used to model the residual effects with the on-axis instrument line shape. This approach is extended to the broad-band case using filter banks. The technique is applied to simulated spectra for the Tropospheric Emissions Spectrometer (TES). This approach is shown to maintain a radiometric accuracy to less than 0.1%.

1 Introduction

High-resolution imaging Fourier transform spectrometers have become an increasingly important tool for a variety of remote sensing applications including astronomy [7] and space-based chemical remote sensing [10, 2, 11, 9]. The Tropospheric Emission Spectrometer (TES) [3] is a polar sun-synchronous FTS that is designed to measure the global chemical state of the troposphere. It has a spectral range of 3.3–15.4 μm and a maximum spectral resolution of 0.025 cm^{-1} [2]. TES has two viewing modes: the nadir mode, which looks down toward the surface, and limb mode, which looks horizontally across the atmosphere. The nadir mode has a maximum optical path difference (OPD) of 8.44696 cm^{-1} and the limb has a maximum OPD of 33.78784 cm. TES has limited imaging capability along one dimension with 16 pixels that have a spatial resolution of 0.5×5 km in the nadir mode and 2.5×23 km in the limb mode.

The retrieval of this chemical state requires two basic steps, denoted as Level 1B and Level 2 [1]. In Level 1B, interferograms measured by TES are processed to produce calibrated spectra. In Level 2, these spectra are compared to a model spectrum generated from an initial guess of the atmospheric state. The parameters specifying

the atmospheric state are iteratively corrected until the model spectrum matches the measured spectrum.

In order for the model spectrum to correctly match the measured spectrum, the effects of the FTS on the line shape and position of the spectra must be either corrected by calibration or included in the calculation of the model spectrum. In particular, the optical geometry of an imaging FTS leads to a number of effects on the spectral line shape and position that must be characterized. In an ideal Fourier transform spectrometer, an interferogram is measured with an on-axis point detector. In this case, there is a simple, linear relationship between the distance traversed by one arm of the interferometer and the optical path of the incident radiation. For a detector of finite dimensions, however, the relationship between the interferometer arm length and the optical path of a ray becomes more complicated due to the off-axis angles subtended.

The off-axis geometry for TES is shown in Figure (1)(a). Spectra measured by off-axis detectors are altered in several ways. Figure (2)(b) shows one side of a uniformly illuminated, symmetric interferogram of a simulated monochromatic input radiance at $\nu = 2537.5 \text{ cm}^{-1}$ measured off-axis by pixel 8 and Figure (2)(a) shows interferogram of the same input radiance measured on the optical axis. The off-axis interferogram is generated by calculating rays across the pixel with a pixel response described in Figure (1)(b). Figure (2)(c) shows the Fourier transform of the on-axis and off-axis interferograms in the limb mode. The off-axis interferogram in Figure (2)(b) appears to be a cosinusoid modulated by some envelope function. The interferogram is referred to as being "self-apodized" since the off-axis geometry itself appears to impose an apodization function on the interferogram [4]. The self-apodization of the interferogram results in an ILS that is broadened in frequency and reduced in amplitude, as shown in Figure (2)(c). In addition, the instrument line shape (ILS) appears to be shifted in frequency and the side-lobes of the ILS are asymmetric. These four characteristics are deviations from the monochromatic input radiance measured on-axis. The first three characteristics are a direct result of measurement with an extended detector. These characteristics are well-understood for a finite and circular field stop [5, 4]. The asymmetry in the line shape, however, is due to the detectors having a rectangular shape rather than being a square. All of these characteristics must be corrected in Level 1B or modeled in Level 2.

The rest of the paper will describe a methodology for correcting and modeling the off-axis effects on the spectrum. An analysis of the off-axis geometry will show how the afore mentioned characteristics can be separated. For narrow-band spectra, the self-apodization, frequency scaling, and line broadening effects may be corrected in the calibration process whereas the asymmetry must be modeled in Level 2. This approach can be extended to broad-band spectra by dividing the spectra using filter banks into smaller frequency bands and then applying corrections to those bands. The methodology will then be applied to a broad-band spectrum for the TES optical geometry.

2 Analysis of off-axis geometry

Figure (1)(a) shows the path of a ray to a pixel positioned off-axis. The output of the detector is equal to the integral over all incident rays weighted by the pixel response

function and over all wavelengths. The interferogram is related to the input spectrum by

$$I(x) = \int_{-\beta_w}^{\beta_w} \int_{\alpha_i}^{\alpha_{i+1}} \left[\int_{-\infty}^{\infty} B(\alpha, \beta) P(\alpha, \beta) L(v) e^{-i2\pi \cos(\phi(\alpha, \beta)) vx} dv \right] d\alpha d\beta, \quad (1)$$

where $B(\alpha, \beta)$ is the illumination across the pixel, $P(\alpha, \beta)$ is the angular response of the detector, $L(v)$ is the input spectrum, α_i and α_{i+1} are the angles to the lower and upper edge of the i th pixel, and β_w is the angle to the maximum horizontal extent of the pixel. The angle of a ray, denoted by ϕ , is related to the angles α and β by

$$\tan^2 \phi = \tan^2 \alpha + \tan^2 \beta. \quad (2)$$

Equation (1) can be interpreted as an interferogram that is equal to a sum of interferograms generated by each ray of incident radiance. Thus, a given distance traversed by the interferometer arm, say \bar{x} , now corresponds to rays summed over slightly different optical paths.

Alternatively, the measured off-axis spectrum can be related to the input spectrum by changing the order of the integration and setting $v' = \cos(\phi(\alpha, \beta))v$. Equation (1) is then written as

$$I(x) = \int_{-\infty}^{\infty} \left[\int_{-\beta_w}^{\beta_w} \int_{\alpha_i}^{\alpha_{i+1}} \frac{B(\alpha, \beta) P(\alpha, \beta)}{\cos(\phi(\alpha, \beta))} F\left(\frac{v'}{\cos(\phi(\alpha, \beta))}\right) d\alpha d\beta \right] e^{-i2\pi v' x} dv'. \quad (3)$$

The off-axis spectrum is simply the kernel of the Fourier transform in Equation (3), or

$$R(v) = \int_{-\beta_w}^{\beta_w} \int_{\alpha_i}^{\alpha_{i+1}} \frac{B(\alpha, \beta) P(\alpha, \beta)}{\cos(\phi(\alpha, \beta))} F\left(\frac{v'}{\cos(\phi(\alpha, \beta))}\right) d\alpha d\beta. \quad (4)$$

From Equation (4), the off-axis spectrum is equal to the sum of input radiances scaled by the factor $1/\cos(\phi(\alpha, \beta))$ where each input radiance corresponds to a separate ray. For $\cos(\phi(0, 0)) = 1$ and $P(0, 0) = 1$, the ray is on-axis and the input spectrum is now equal to the measured spectrum. Note that $\cos(\phi(\alpha, \beta)) \leq 1$, which reflects the fact that for a given arm length, the optical path difference (OPD) of off-axis rays is always less than the OPD of on-axis rays. As a consequence, the measured spectrum is always scaled toward lower frequencies relative to the input spectrum.

With some simplifying assumptions on Equation (1), these off-axis effects can be separated into terms. For $\phi < 10$ mrad, which is the maximum off-axis angle, ϕ approximates $\tan \phi$ to within 11 significant digits. Therefore, Equation (2) can be approximated by

$$\phi^2 \approx \alpha^2 + \beta^2, \quad (5)$$

and thus

$$\cos \phi(\alpha, \beta) \approx 1 - \frac{\alpha^2 + \beta^2}{2}. \quad (6)$$

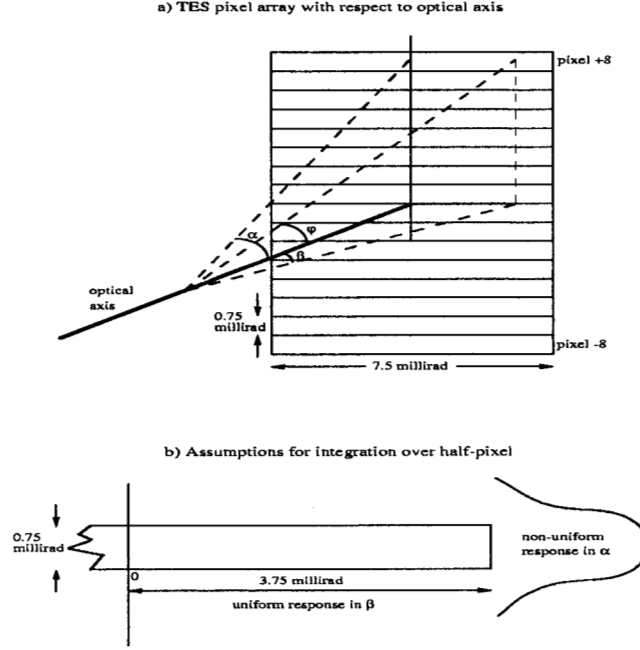


Figure 1: Off-axis geometry and assumed pixel response function for TES detectors.

Substituting Equation (6) into Equation (1) leads to

$$I(x) \approx 2\text{Re} \left\{ \int_0^\infty L(v) A(vx) e^{-i2\pi vx} dv \right\}, \quad (7)$$

where

$$A(vx) = \int_{-\beta_w}^{\beta_w} \int_{\alpha_i}^{\alpha_{i+1}} B(\alpha, \beta) P(\alpha, \beta) e^{i2\pi\alpha^2 vx} e^{i2\pi\beta^2 vx} d\alpha d\beta. \quad (8)$$

The function $A(vx)$ is called the *Fresnel kernel*. The Fresnel kernel completely describes the effects of the off-axis geometry on the interferogram and spectrum.

The Fresnel kernel can be written in phaser form as

$$A(vx) = |A(vx)| e^{i\Phi(vx)}. \quad (9)$$

For $v = 2537.5 \text{ cm}^{-1}$ and pixel 8, the magnitude and phase of the Fresnel kernel is shown in Figure (3). The magnitude of the Fresnel kernel in Figure (3)(a) corresponds to the envelope or “self-apodization” of the off-axis interferogram shown in Figure (2). Hence, the Fresnel magnitude function is called the *self-apodization function*. The

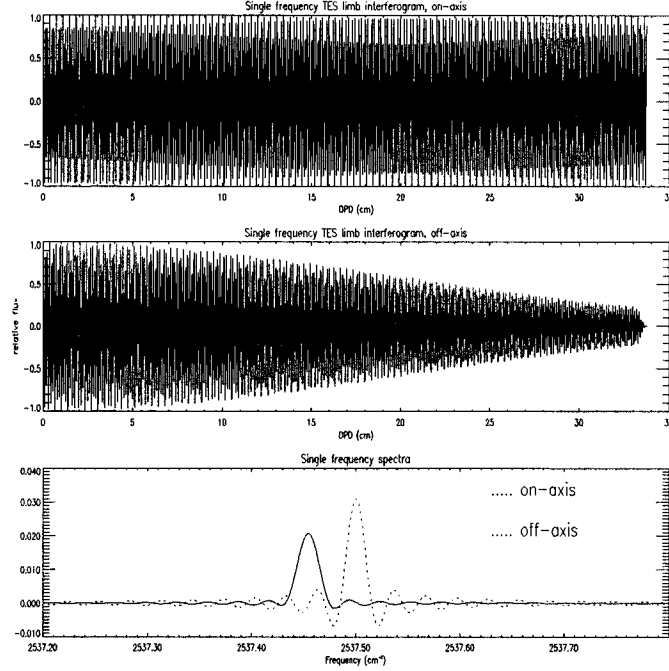


Figure 2: (a) Simulated on-axis interferogram for a limb view at pixel 8. (b) Simulated off-axis interferogram measured at pixel 8. The off-axis interferogram decreases in amplitude with OPD. (c) The ILS for a spectrum measured on-axis and off-axis. The off-axis spectrum is attenuated in amplitude, asymmetric about the center frequency, line-broadened, and shifted down in frequency with respect to the on-axis ILS for the same input frequency.

phase function of the Fresnel kernel, shown in Figure (3)(b), is dominated by a linear term. The slope of this term corresponds to the frequency shift shown in Figure (2)(c).

This phase function, however, is non-linear. The Fresnel phase function can be decomposed into linear and non-linear components, denoted as

$$\Phi(vx) = 2\pi\rho vx + \psi(vx). \quad (10)$$

Substituting Equation (9) and Equation (10) into Equation (7) leads to

$$I(x) = 2\text{Re} \left\{ \int_0^\infty |A(vx)| e^{i\psi(vx)} L(v) e^{-i2\pi(1-\rho)vx} dv \right\}. \quad (11)$$

For a narrow band spectrum the self-apodization function and the non-linear component of the phase function can be approximated as a constant function of frequency.

Denoting the mean frequency as $\bar{\nu}$, Equation (11) becomes

$$I(x) \approx 2|A(\bar{\nu}x)|\text{Re} \left\{ e^{i\psi(\bar{\nu}x)} \int_0^\infty L(\bar{\nu}) e^{-i2\pi(1-\rho)\bar{\nu}x} d\nu \right\} \quad (12)$$

$$\approx 2|A(\bar{\nu}x)|\text{Re} \left\{ e^{i\psi(\bar{\nu}x)} I_L \left(\frac{x}{1-\rho} \right) \right\}, \quad (13)$$

where $I_L(x)$ is interpreted as an interferogram measured on-axis. The first term in Equation (12) is the self-apodization function and the second term represents the non-linear portion of the Fresnel phase function. This phase function, $\psi(\bar{\nu}x)$, is called the *residual Fresnel phase function* or simply the *residual phase function*. The residual phase function is shown in Figure (4)(a). The term $e^{i\psi(\bar{\nu}x)}$ is treated as a complex ILS function and is called the *residual ILS function*. The Fourier transform of the residual ILS function is shown in Figure (4)(b). The side-lobes depicted in Figure (4)(b) are asymmetric. Hence the convolution of the Fourier transform of the residual ILS function with a monochromatic input will also result in asymmetric side-lobes of the spectrum as shown in Figure (2)(c). Finally, the spectrum is scaled by $1/(1-\rho)$. The slope of the Fresnel phase function, ρ , is also called the *off-axis compression factor* and the term $(1-\rho)$ is the *off-axis scale factor*. What appears to be a shift in Figure (2)(c) is actually a scaling.

The Fresnel kernel described in Equation (8) and in Equation (12) capture the observed features of off-axis spectra:

- the magnitude of the Fresnel kernel describes the envelope of the interferogram as well as the broadening and the decrease in amplitude of the spectrum,
- the non-linear phase term of the Fresnel kernel describes the asymmetry of the spectrum,
- the linear phase term of the Fresnel kernel describes the scaling of the input radiance.

3 Correction and modeling for narrow-band spectra

The expression of the interferogram in Equation (12) becomes the basis for the correction and modeling of narrow-band spectra. For a narrow frequency band, we can ignore the frequency dependence of the self-apodization and residual ILS function. With this approximation, self-apodization term can be simply divided out of the interferogram. The residual ILS function, on the other hand, will have to be modeled in Level 2 because it is a complex function and therefore can not be removed from inside the real operator. The scaling of the spectrum can be removed by rescaling the frequency axis and interpolating onto the on-axis frequency grid using an FFT signal-interpolation method [8].

The steps used to test this approach are shown in Figure (6). For a given pixel, an off-axis interferogram is generated by evaluating Equation (7) with the Fresnel kernel defined in Equation (8). The interferogram is then divided by the self-apodization

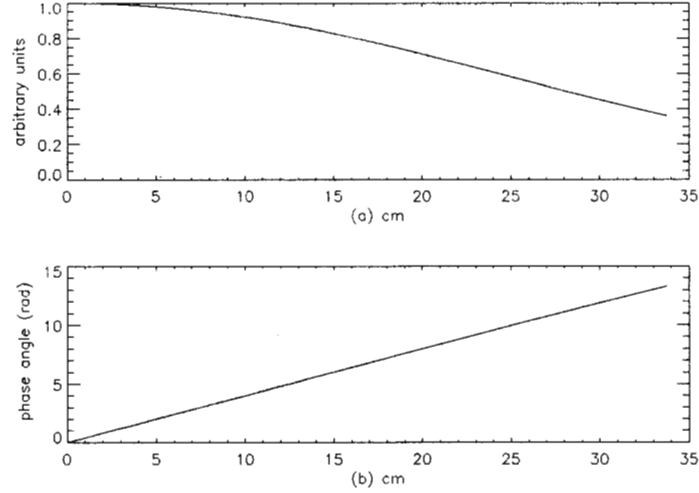


Figure 3: (a) The magnitude of the Fresnel kernel (b) the phase of the Fresnel kernel for $\nu = 2537.5 \text{ cm}^{-1}$

function. The interferogram is transformed into spectral space and the frequency scale corrected. The spectrum is subsequently interpolated onto the on-axis frequency grid resulting in the Level 1B corrected spectrum. In this case, the spectrum is assumed to have been previously calibrated. In Level 2, a model interferogram is multiplied by the residual ILS function, which was calculated from the Fresnel kernel, and then transformed into spectral space. The Level 2 model spectrum is then compared with the Level 1B corrected spectrum.

These steps are illustrated in Figure (7) for a spectrum measured from pixel 8. The calculation of the Fresnel kernel assumes uniform illumination and a uniform pixel response along the length with a response along the height depicted in Figure (5). By symmetry, only half the length along the pixel needs to be integrated. The integration was performed using 100 points for the length and 21 points for the width. The pixels are assumed to be adjacent with no gaps and the optical axis is assumed to bisect pixels -1 and 1. The errors for each of the major steps is shown in Table (1) for three different frequency regimes. For TES, the total radiometric accuracy is required to be better than 1%. We have chosen 0.1% radiance as the maximum tolerable error for the difference between the corrected Level 1B spectrum and the Level 2 spectrum with the residual ILS model. This radiometric accuracy requirement is satisfied for frequency bands smaller than 10 cm^{-1} . In atmospheric retrievals, narrow-band spectra, i.e., micro-windows, are frequently used to estimate the chemical state. For these cases, the correction approach based on a monochromatic frequency is adequate. However, for broad-band spectra, this technique must be extended via filter banks.

Table 1: Error levels for ILS correction & modeling processing steps using simulated limb views for pixel 1 (8th off-axis pixel). Center of range used as correction frequency. For simulated limb spectra, the error is defined as the maximum difference divided by the average signal.

Frequency range (cm^{-1})	Processing step	max. error/ avg. signal
2459-2464	L1B correction - uncorrected	10%
2459-2464	on-axis (no L2 model) - L1B	3%
2459-2464	on-axis with L2 model - L1B	0.05%
1047.5-1052.5	L1B correction - uncorrected	5.5%
1047.5-1052.5	on-axis (no L2 model) - L1B	0.3%
1047.5-1052.5	on-axis with L2 model - L1B	0.024%
1040-1060	L1B correction - uncorrected	6%
1040-1060	on-axis (no L2 model) - L1B	0.3%
1040-1060	on-axis with L2 model - L1B	0.14%

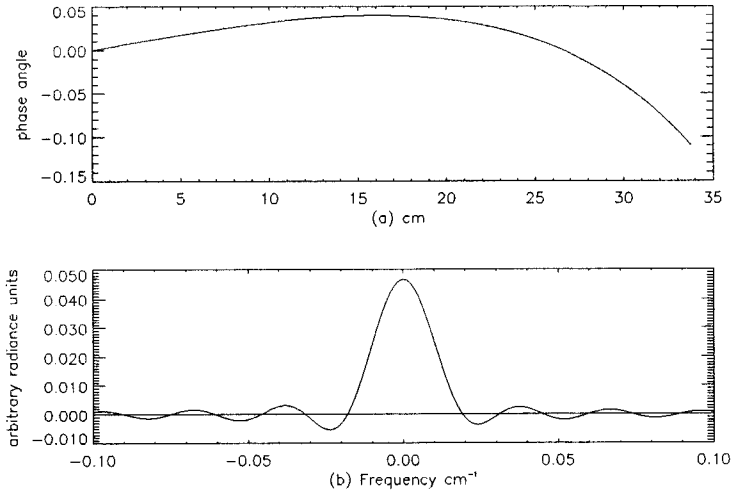


Figure 4: (a) The residual Fresnel phase function (b) The Fourier transform of the residual ILS function

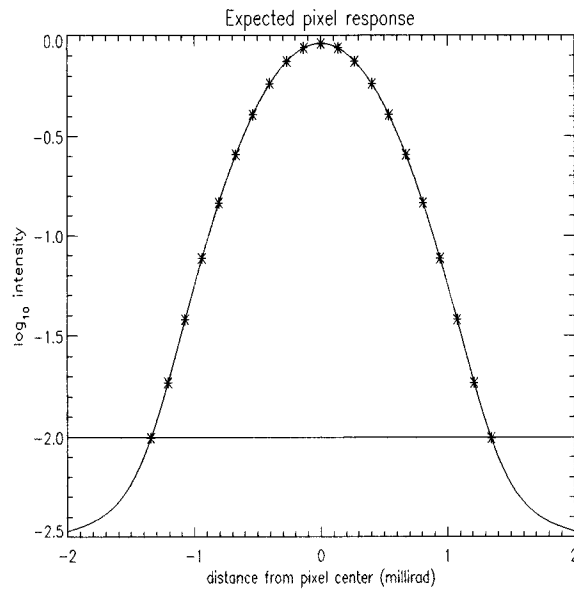
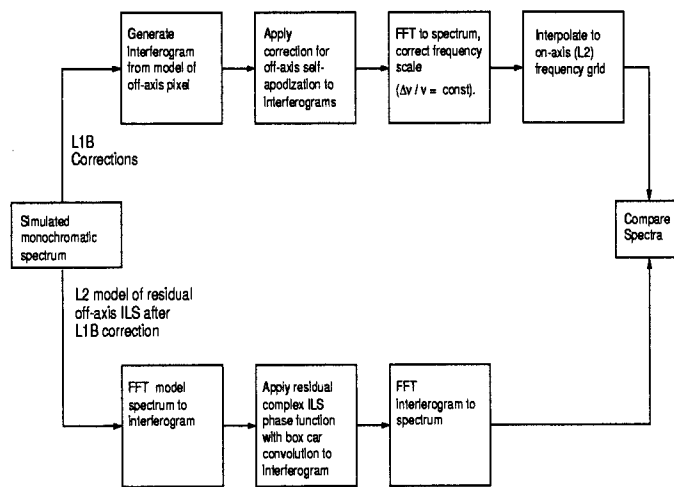


Figure 5: Expected pixel response along array axis. Although the physical width of each pixel is 0.75 millirad, the response is wider than this due to diffraction and charge diffusion. Stars represent the points included in the interferogram model integration. (Angles corresponding to intensities lower than 2db below the maximum were not included).

Test of Off-Axis ILS Correction and Modeling



H. Worden 09/30/97

Figure 6: Validation steps for off-axis ILS correction and modeling algorithms.

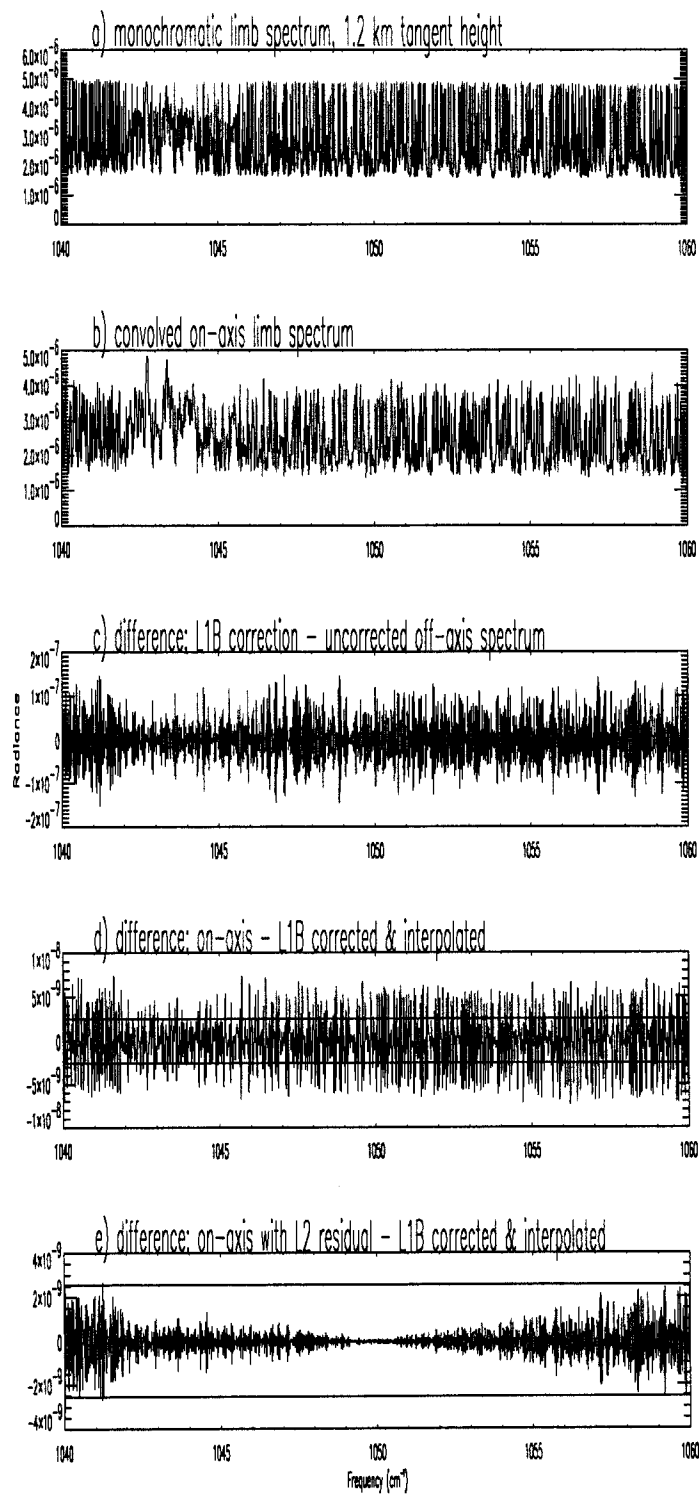


Figure 7: Spectra and spectral differences at different stages in the off-axis ILS correction/residual modeling. Horizontal lines in plots e & f indicate 0.1% error level.

4 Correction and modeling for broad-band spectra

For frequency bands of width less than 10 cm^{-1} , we can neglect the frequency dependence of the Fresnel kernel in Equation (12). This technique can be extended to a broad-band spectrum by splitting the spectrum into narrow frequency bands. The input spectrum is then represented as

$$L(\nu) = L_1(\nu) + L_2(\nu) + \cdots + L_M(\nu), \quad (14)$$

where M is the number of bands and $L_n(\nu)$ is non-zero only on the interval $\nu \in [\nu_n, \nu_{n+1}]$. Equation (14) is equivalent to passing the spectrum through a contiguous set of ideal narrow band-pass filters. Each of the interferograms, $I_1(x), I_2(x), \dots, I_M(x)$ corresponding to the frequency bands, can be modeled by Equation (13). The self-apodization and residual ILS functions are calculated for the frequencies defined by

$$\bar{\nu}_n = \frac{\nu_n + \nu_{n+1}}{2}, \quad (15)$$

which is the center of the band.

The principle problem, however, is to calculate $I_n(x)$ in the first place. Moreover, it must be possible after the correction for self-apodization to reconstruct the complete interferogram $I(x)$. In the absence of any correction, this reconstruction should be perfect. There exists an efficient technique known as “filter banks” (or wavelets) that can efficiently split a spectrum into bands in such a way as to allow for perfect reconstruction from those bands [12, 6].

4.1 Filter banks

Filter banks are a means of splitting a signal into frequency subbands. The principle advantage of filter banks over other filtering techniques is that the signal can be reconstructed *perfectly* from its subband components. In fact, filter banks are generally orthogonal or biorthogonal transformations. In addition to (bi)orthogonality, the computational efficiency of filter banks is comparable to a fast Fourier transform (FFT).

A simple, 2-channel filter bank is shown in Figure (8). The filter bank is composed of linear time-invariant (LTI) filters, downsamplers, and upsamplers. The interferogram, denoted by $I[n]$, is convolved with the impulse response functions, $h_0[n]$ and $g_0[n]$, of low and high pass filters, respectively. The magnitudes of the frequency response of g_0 and h_0 are shown in Figure (9). The impulse response functions for these filters are listed in Table (2).

After convolution, the signals are then downsampled. For the two-band case, the downsampler operator is defined as [8]

$$(\downarrow 2I)[n] = I[2n]. \quad (16)$$

Thus, the signal lengths of the high-passed and low-passed interferograms are cut in half and the band-width of both interferograms is reduced by a half. If the input signal is not sufficiently band-limited, then the downsampling operation will cause aliasing. The filters in Figure (8) are designed, however, to insure that this aliasing does not

occur. The filters and downsamplers on the left side of the vertical dash in Figure (8) comprise the *analysis* part of the filter bank.

The *synthesis* part of the filter bank, which is on the right side of the vertical dash, is composed of upsamplers and filters. For the two-channel case, an upsampler is defined as [8]

$$(\uparrow 2)I[n] = \begin{cases} I[\frac{n}{2}] & n = 0, \pm 2, \pm 4, \dots \\ 0 & \text{otherwise.} \end{cases} \quad (17)$$

The upsampling operator scales the spectrum of the signal by a factor of 2.

After the upsampling operation, the low-pass and high-pass signals are then filtered again by $h_1[n]$ and $g_1[n]$, respectively. The output signals of the filtering operation are then recombined.

For certain h_0 , h_1 , g_0 , and g_1 , the recombined signal will be the same as the input signal. The filter bank is then said to be a *perfect reconstruction* filter bank. We will restrict our attention to finite impulse response (FIR) biorthogonal linear-phase filter banks [6, 12]. Filter banks based on FIR filters are computationally efficient. Biorthogonal, linear-phase filters are used to insure so that the symmetry of the interferograms and the phase of their spectra are unchanged.

It should be pointed out that Figure (8) shows the filter bank at a conceptual level. Filter banks are *not* implemented as filters followed by downsamplers. Instead, the input signal is separated into even and odd components. When this is done, the downsamplers in the analysis bank can be interchanged with the filters. Restructuring the filter bank in this way is known as a *polyphase* implementation [12]. This form of the filter bank is very efficient. For FIR filters with filter coefficients of length M and an input signal of length N ,

$$\text{operations needed to generate output of analysis bank} < 2MN. \quad (18)$$

An FFT, on the other hand, requires $O(N \log N)$ multiplications. Thus, for filters with a small number of coefficients, filter banks can actually be computed faster than an FFT.

The properties of the 2-channel case can be easily extended to higher channels. Figure (10) shows the analysis part of a 4-channel filter bank. The low-pass and high-pass components of the first stage are split again into smaller frequency bands. Since each stage of the analysis bank can be perfectly reconstructed from the same stage in the synthesis bank, the entire filter bank maintains the perfect reconstruction property.

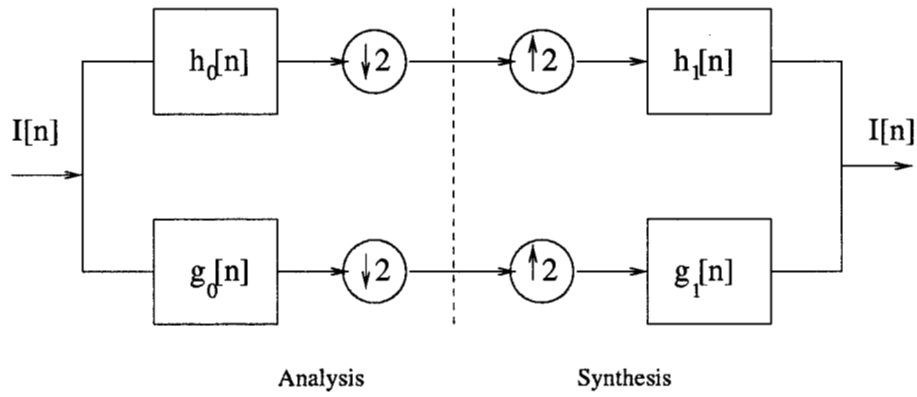


Figure 8: 2-channel filter bank

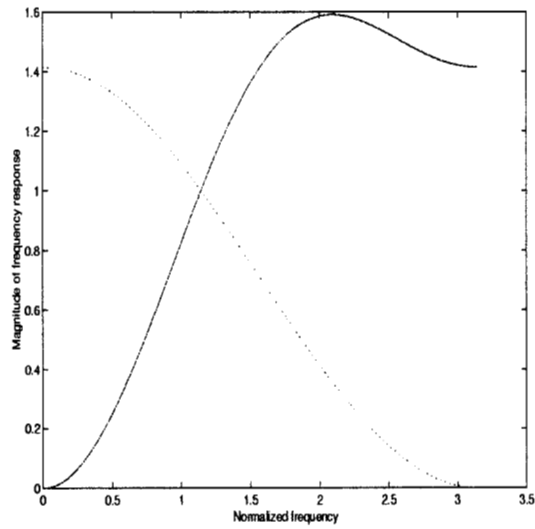


Figure 9: Frequency response of the biorthogonal filters. The low-pass frequency response is $H_0(\omega)$ and the high-pass frequency response is $G_0(\omega)$.

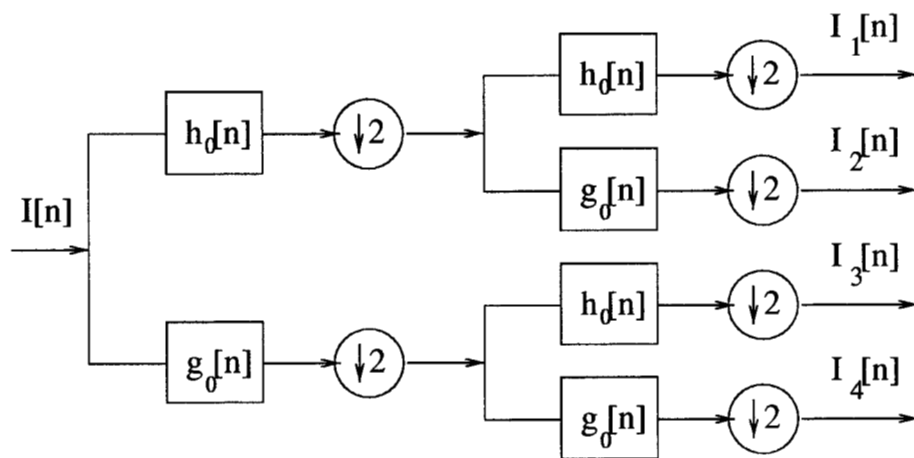


Figure 10: 4-channel filter bank based on iterating the 2-channel case. Only the analysis bank is shown. The synthesis bank is simply the reverse of the analysis bank where the downsamplers are replaced by upsamplers.

4.2 Correction and modeling for two-band case

The testing procedure and description of the off-axis ILS correction and modeling algorithm is similar to the narrow-band case shown in Figure (6) except that the measured off-axis interferogram and the Level 2 model interferogram are split into a set of interferograms using filter banks.

Figure (11) shows the processing steps for Level 1B for a two-band case. The approach can be extended to a greater number of channels in a straight-forward manner. First, the spectrum is radiometrically calibrated. Then, the measured interferogram is split into two interferograms that represent the low-pass and high-pass parts of the spectrum, respectively. Thus, these two interferograms, $I_1[n]$ and $I_2[n]$, correspond to the frequency bands in Equation (14). The self-apodization term in Equation (12) is divided out from both interferograms and then recombined into two interferograms. Finally, the interferogram is resampled at the rate of the scale factor. The Level 1B output interferogram $I_{L1B}[n]$ still has the residual ILS terms, which must be removed in Level 2.

Figure (12) shows the processing steps for Level 2. The forward model interferogram, $I_F[n]$, is split into a low-pass interferogram $I_{F,1}[n]$ and a high-pass interferogram $I_{F,2}[n]$. Each interferogram is then multiplied by a residual ILS function evaluated at $\bar{\nu}_1$ and $\bar{\nu}_2$, respectively. The resulting interferograms are then recombined to produce $I_{L2}[n]$. Ideally, the difference between $I_{L2}[n]$ and $I_{L1B}[n]$ is negligible.

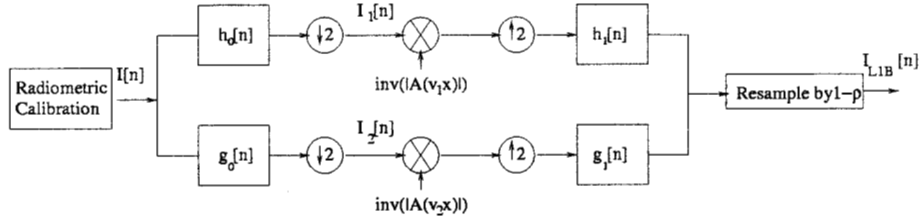


Figure 11: Level 1B processing: The functions $h_0[n]$ and $h_1[n]$ refer to low-pass filters while $g_0[n]$ and $g_1[n]$ refer to high-pass filters. The uparrows and downarrows refer to upsampling and downsampling, respectively.

This technique was tested for a simulated limb spectrum over a spectral region between $1040 - 1060 \text{ cm}^{-1}$. An off-axis interferogram was modeled using Equation (7) for the 8th off-axis detector element assuming uniform illumination. The Fresnel kernel was calculated for $\bar{\nu}_1 = 1045 \text{ cm}^{-1}$ and $\bar{\nu}_2 = 1055 \text{ cm}^{-1}$. The off-axis compression factor for both Fresnel kernels was $\rho = 1.818 \times 10^{-5}$. The magnitudes of the Fresnel kernels and their non-linear phases are shown in Figures (13) and (14). The filter bank coefficients for $h_0[n]$ and $h_1[n]$ are shown in Table (2). The coefficients for $g_0[n]$ and $g_1[n]$ can be calculated directly from $h_0[n]$ and $h_1[n]$ [12]. Note that we have only listed half of the coefficients for each filter. These filters are symmetric about the first elements in Table (2). The spectrum produced from Level 1B processing for this case is shown in Figure (15). The error between the on-axis spectrum and the Level 1B

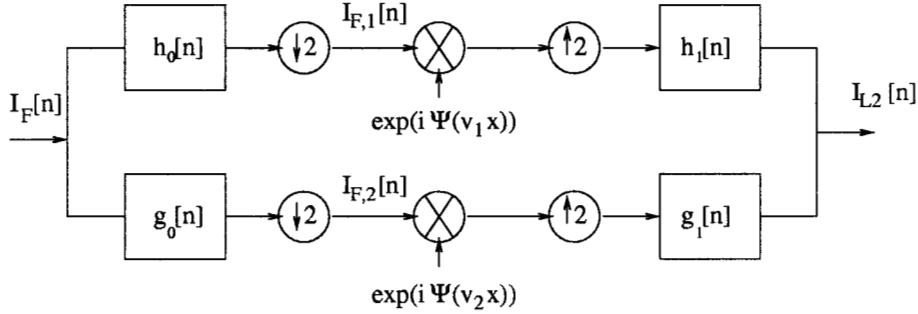


Figure 12: Level 2 processing

corrected spectrum is defined as

$$\epsilon = \frac{\max(|L_{on-axis}(\omega) - L_{L1B}(\omega)|)}{\text{mean}(L_{on-axis}(\omega))}. \quad (19)$$

In this case, $\epsilon_{1B-only} = .00289$, which is roughly a .3% error. The on-axis interferogram is now multiplied by the residual ILS functions via the filter banks in Figure (12). The resulting spectrum is compared to the output of the Level 1B processing, which is shown in Figure (16). The error between the Level 1B processing and Level 2 is now $\epsilon_{combined} = .000519$, which is over a factor of 5 improvement than just doing the Level 1B processing alone. Moreover, this systematic error, which is around .05% is quite acceptable compared to the estimated measurement error of .36% for the 1B2 filter in the tropics [1].

Table 2: Filter bank coefficients

h_0	.383269
	.767245
	.383269
	-.068867
	-.033475
	.047282
	.003759
	-.008473
h_1	.832848
	.448109
	-.069163
	-.108737
	.006292
	.014182

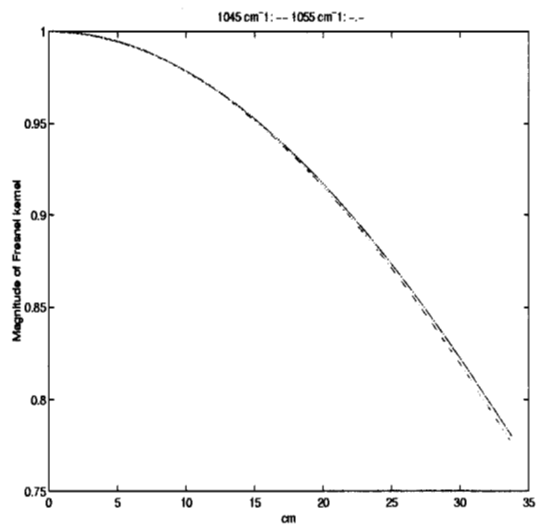


Figure 13: Magnitude of the Fresnel kernel, which is also called the self-apodization function, for 1045 and 1055 cm^{-1} .

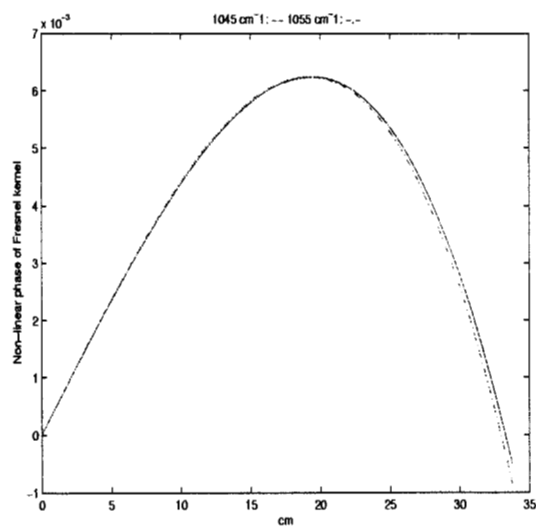


Figure 14: Residual Fresnel phase function for 1045 and 1055 cm^{-1} . The complex exponent of these functions are the residual ILS functions.

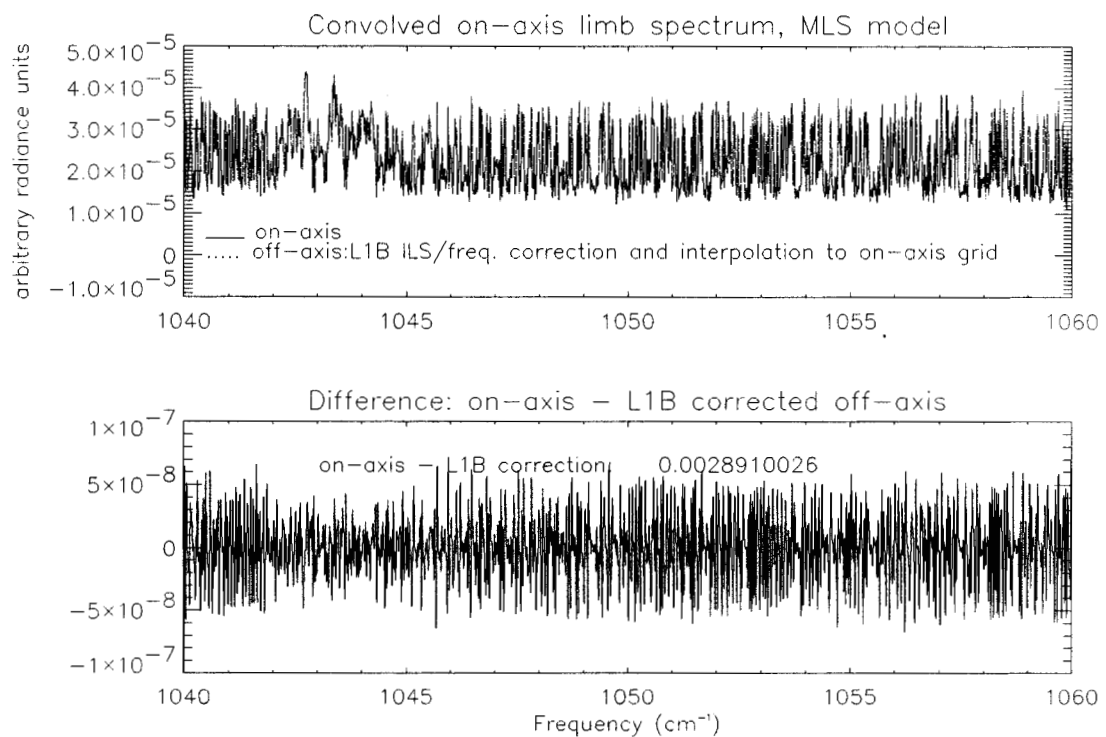


Figure 15: Comparison between on-axis spectrum and the off-axis spectrum after Level 1B correction. The off-axis spectrum was split into two subbands using filter banks. The self-apodization functions were applied respective interferograms of the subbands. The subbands were reconstructed and then scale corrected. The error stated above the difference plot is defined as the maximum difference between the on-axis and Level 1B corrected off-axis divided by the mean value of the on-axis spectrum.

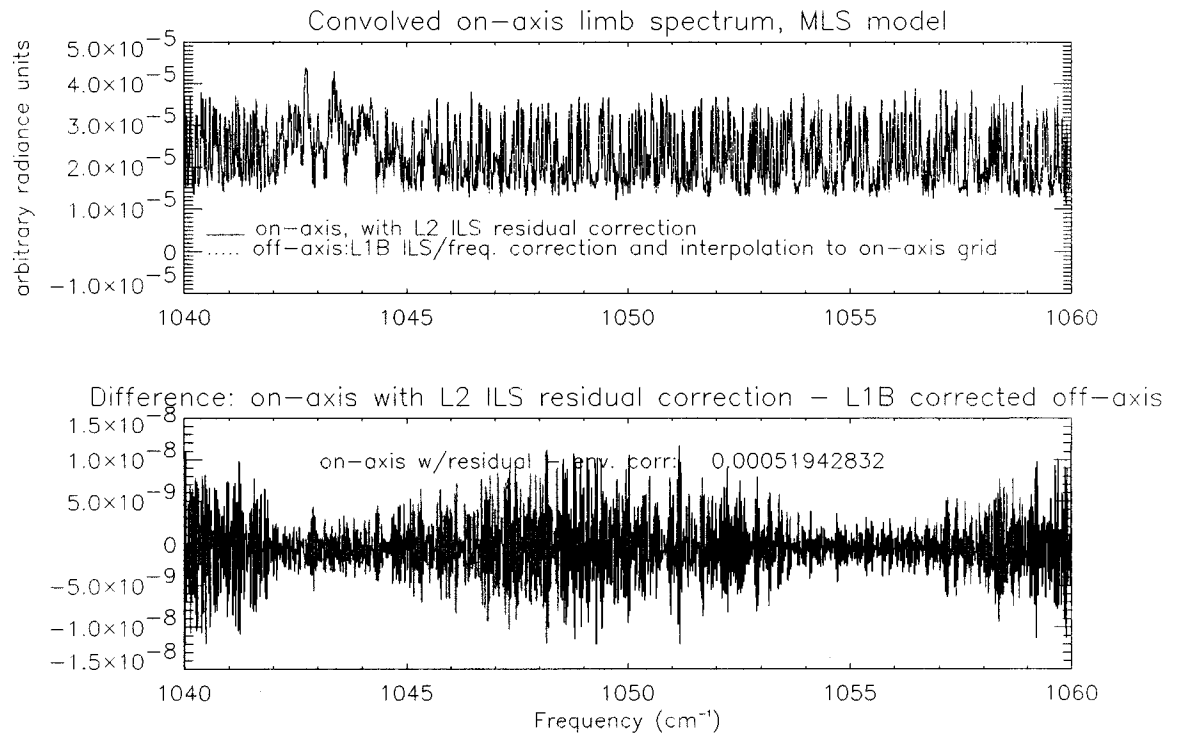


Figure 16: Comparison between the on-axis spectrum with the residual ILS functions and the off-axis spectrum after Level 1B correction. The error increases for spectral points that are farther away from the correcting frequencies.

5 Non-uniform illumination

The previous examples have assumed a known, uniform illumination over the pixel. In practice the actual illumination can vary and is generally not known. To test the sensitivity of the method to illumination errors we calculated a gradient illumination, which was assumed to be constant in the horizontal direction but drops off linearly from one to zero in the vertical direction. This represents a “worst case” situation, but has similarities to a pixel viewing the tropopause in either its upper or lower edge. Figure (17) shows the effective pixel response under gradient illumination. The Fresnel kernel was calculated for both uniform and gradient illumination for 1050 cm^{-1} .

The Fresnel kernel calculated for the gradient illumination was applied to the off-axis spectrum described in Figure (7) under uniform illumination. The corrections were made over a 5 cm^{-1} window. The errors for the uniformly and gradient illuminated case are shown in Table (3). For the uniform case, there are no model errors and thus they establish a baseline. For the gradient case, the error in the Level 1B correction increases by approximately a factor of 2. This error, however, is still considered acceptable. The Level 2 residual correction, on the other hand, is an order of magnitude worse than the Level 1B correction only. In this case, it would be better to not apply the Level 2 residual modelling at all. The explanation for this performance can be seen by examining the change in the self-apodization and residual ILS phase functions, which are shown in Figure (18). The self-apodization function has only a slight variation with illumination whereas the residual ILS phase function has changed significantly.

The variation of the illumination appears to change the slope of the residual ILS function. This suggests that the residual ILS function could be parameterized as a function of the field-of-view (FOV) illumination, which is estimated during the retrieval. From the estimated FOV, the residual ILS function could be calculated, leading to a more robust algorithm. The effect of illumination on the ILS underscores the importance of separating the self-apodization correction in Level 1B and the residual modeling in Level 2. The Level 1B correction allows the spectra from all of the pixels to be intercompared even in the presence of non-uniform illumination between the pixels. Modelling the ILS entirely does not allow one to separate those ILS effects insensitive to non-uniform illumination from those effects that are sensitive to non-uniform illumination.

Table 3: Error levels for ILS correction & modeling processing steps using simulated limb views for pixel 1 (8th off-axis pixel) for both the cases of known (uniform) illumination and illumination mismatch (gradient).

Illumination	Processing step	max. error/ avg. signal
Uniform	on-axis (no L2 model) - L1B	.27%
Uniform	on-axis with L2 model - L1B	0.024%
Gradient	on-axis (no L2 model) - L1B	0.56%
Gradient	on-axis with L2 model - L1B	5.6%

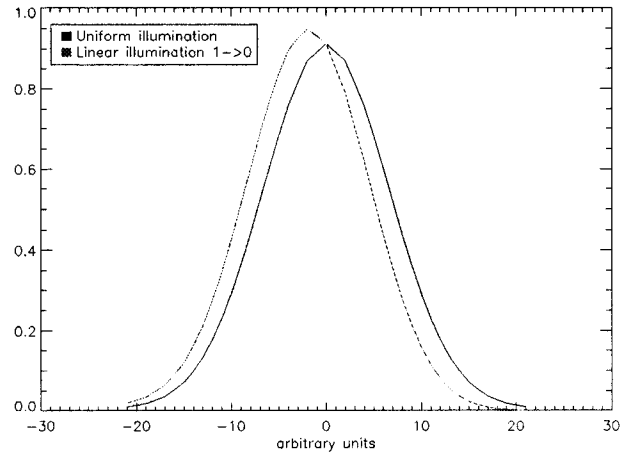


Figure 17: Pixel response of the detector under non-uniform and gradient illumination.

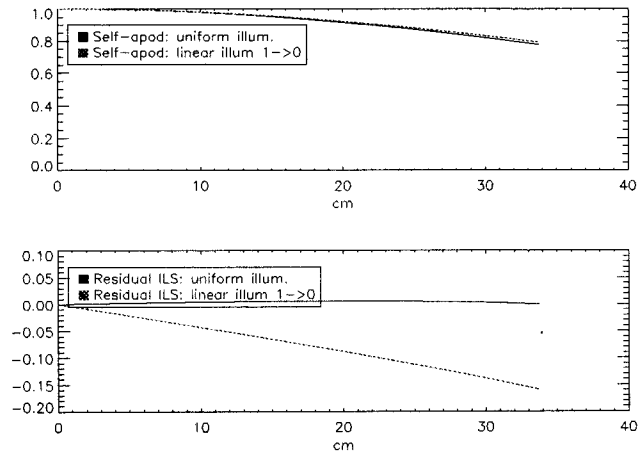


Figure 18: The self-apodization functions and residual ILS phase functions under uniform and non-uniform illumination.

6 Conclusions

A technique has been described that corrects and models the instrument line shape for an off-axis detector geometry in an imaging Fourier transform spectrometer. This geometry induces self-apodization, frequency scaling, line broadening, and asymmetry to the line shape. For off-axis pixels that subtend small incident rays of radiation, the effects of the off-axis geometry on the instrument line shape can be described by the Fresnel kernel. The magnitude of the Fresnel kernel corresponds to the self-apodization and line-broadening while the phase of the Fresnel kernel corresponds to the frequency scaling and asymmetry. It was shown that the self-apodization, line broadening, and frequency scaling can be removed in the Level 1B calibration processing whereas the term associated line shape asymmetry must be modeled in Level 2.

The off-axis ILS algorithm was applied to narrow-band and broad-band spectra. For spectra with bandwidths less than 10 cm^{-1} , a direct application of the off-axis formalism is sufficient to achieve a .1% radiometric accuracy. For greater spectral bandwidths, the technique of filter banks was used to split a spectrum into small bands. The formalism could then be applied separately to each band. This technique was applied to a spectrum with a bandwidth of 20 cm^{-1} . For the two-band case, the radiometric error was approximately .05%. It was also shown how this technique can be extended to correction and modeling of off-axis spectra greater bandwidths in a straight-forward manner.

The sensitivity of non-uniform illumination on this technique was also examined. In particular, we examined the case of a vertical gradient in the illumination. We found that the Level 1B correction is relatively insensitive to changes in illumination but the Level 2 residual corrections are sensitive to illumination. This result confirms the need of separating Level 1B corrections from modeling residual effects in Level 2. We suggest using the relative radiance distribution across the FOV that is estimated as part of the retrieval to modify the residual ILS functions thereby accounting for the non-uniform illumination.

References

- [1] R. Beer. Tropospheric Emissions Spectrometer: scientific objectives and approach, goals and requirements. D-11294, JPL, May 1996. Revision 5.0.
- [2] R. Beer and T. Glavich. Remote sensing of the troposphere by infrared emissions spectroscopy. *Applied Optics*, 1129:42–51, 1989.
- [3] R. Beer, T. Glavich, and D. Rider. Tropospheric Emission Spectrometer (TES) for the Earth Observing System (EOS) chemistry I satellite: I objectives, requirements and instrument overview. *Applied Optics*, 1999. Submitted for publication.
- [4] R.J. Bell. *Introductory Fourier Transform Spectroscopy*. Academic Press, New York, 1972.
- [5] J. Chamberlain. *The Principles of Interferometric Spectroscopy*. John Wiley & Sons, New York, London, Sydney, 1979.

- [6] S. Mallat. *A Wavelet Tour of Signal Processing*. Academic Press, New York, 1998.
- [7] J.P. Malliard, D.A. Simons, C.C. Clark, S. Smith, J. Kerr, and S. Massey. CFHT's imaging Fourier transform spectrometer. *SPIE*, 2198:185–193, 1994.
- [8] A. V. Oppenheim and R. W. Schaffer. *Discrete-Time Signal Processing*. Prentice-Hall, Englewood Cliffs, N.J., 1989.
- [9] J. J. Puschell and P. Tompkins. Imaging spectrometers for future earth observing systems. *SPIE*, 3117:36–48, 1997.
- [10] K. Silk and E.R. Schildkraut. Imaging Fourier transform spectroscopy for remote chemical sensing. *SPIE*, 2763:169–177, 1996.
- [11] D. Siméoni, C. Singer, and G. Chalon. Infrared atmospheric sounding interferometer. *Acta Astronautica*, 40:113–118, 1997.
- [12] G. Strang and T. Nyugen. *Wavelets and Filter Banks*. Wellesley-Cambridge Press, Wellesley, 1996.